

Kaleidoscopic Background Attack: Disrupting Pose Estimation with Multi-Fold Radial Symmetry Textures

Xinlong Ding^{*1}, Hongwei Yu^{*1}, Jiawei Li^{*1}, Feifan Li¹, Yu Shang²
Bochao Zou¹, Huimin Ma¹, Jiansheng Chen^{†1}

¹ University of Science and Technology Beijing, China ² Tsinghua University, China

<https://wakuwu.github.io/KBA>

Abstract

Camera pose estimation is a fundamental computer vision task that is essential for applications like visual localization and multi-view stereo reconstruction. In the object-centric scenarios with sparse inputs, the accuracy of pose estimation can be significantly influenced by background textures that occupy major portions of the images across different viewpoints. In light of this, we introduce the Kaleidoscopic Background Attack (KBA), which uses identical segments to form discs with multi-fold radial symmetry. These discs maintain high similarity across different viewpoints, enabling effective attacks on pose estimation models even with natural texture segments. Additionally, a projected orientation consistency loss is proposed to optimize the kaleidoscopic segments, leading to significant enhancement in the attack effectiveness. Experimental results show that optimized adversarial kaleidoscopic backgrounds can effectively attack various camera pose estimation models.

1. Introduction

Camera pose estimation involves determining the positions and orientations of cameras based on multi-view images. The accuracy of these estimates is critical for various downstream tasks, including visual localization [14, 20], multi-view stereo reconstruction [10, 41], and novel view synthesis [23, 27]. Sparse-view object-centric scenes, where objects are centered on a flat surface and imaged by cameras oriented towards them, are among the most common scenarios in practical applications. Classic methods like Structure from Motion (SfM) [1, 9, 31, 38] can not adapt to such scenarios since they require dense viewpoints. Consequently, many learning-based approaches [19, 24, 26, 30, 32, 34, 35, 43, 44] have been proposed to bridge this gap, achieving satisfying performance with sparse views.

However, these learning-based methods often rely on

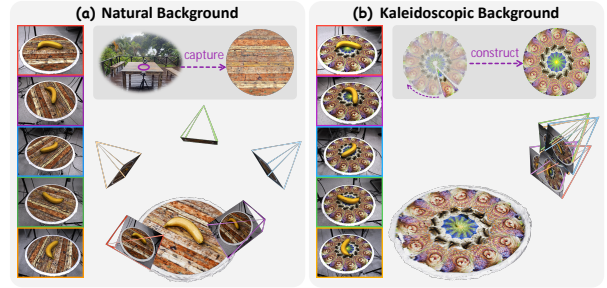


Figure 1. Impact of natural and kaleidoscopic backgrounds on camera pose estimation in object-centric scenes. (a) With a natural tabletop background, the DUST3R model accurately estimates the camera pose and reconstructs the banana. (b) With a kaleidoscopic background, the model predicts erroneous but similar poses across viewpoints, leading to reconstruction failure.

background information that occupies a large portion of the image to accurately estimate camera poses from sparse views. This reliance makes it possible for specific texture patterns to interfere with the model’s output. However, the robustness of pose estimation models under such situations has not been fully discussed previously. In light of this, we aim to explore the vulnerability of such models by leveraging background textures through adversarial attacks.

Since the pioneering study by Szegedy et al. [33], the adversarial robustness of deep neural networks (DNNs) has been extensively studied over the years [6, 11, 13, 15, 22, 25, 28, 42]. Classic patch-based attacks [5, 7, 12, 18, 21, 36], a common form of adversarial attack, often optimize perturbations directly on a standalone patch image, limiting their adaptability in physical environments. Recent studies try to address these limitations by leveraging repeated texture patterns [17, 39] and learnable patch shapes and locations [8, 37], significantly enhancing their success rates in the physical world. This leads us to consider what kinds of texture priors can enhance adversarial attacks for camera pose estimation tasks in the physical world.

We observe that numerous radial symmetric patterns ex-

^{*} Equal contribution. [†] Corresponding author (jschen@ustb.edu.cn).

ist in nature and everyday life [3], such as five-fold starfish, six-fold snowflakes, and various multi-fold patterns like flowers, water splashes, and kaleidoscopes. Such radially symmetric textures enable background similarity across multiple viewpoints. Inspired by this, we select a radially symmetric disc, uniformly divided into several segments, resembling a sliced pizza. Each of the N segments shares the same texture, forming an N -fold radially symmetric kaleidoscopic disc that provides consistent background appearances across multiple viewpoints, as illustrated in Fig. 1(b). We begin with natural textures scanned from a desktop as segments to create the kaleidoscopic disc, referred to as KBA_{nat} in the following sections. Experimental results show that a kaleidoscopic disc constructed solely from natural texture segments can already noticeably impact camera pose estimation across various models.

To further enhance the adversarial impact of the kaleidoscopic background on camera pose estimation, we introduce adversarial attacks to craft the kaleidoscopic segments, resulting in an optimized radially symmetric background, referred to as KBA_{opt} . Specifically, we leverage differentiable rendering techniques [29] to generate diverse multi-view object-centric scenes, incorporating various objects and background environments to simulate real-world scenarios. Building on this, we select a popular camera pose estimation model as a surrogate to conduct adversarial attacks by maximizing camera orientation similarity across different viewpoints. Experiments demonstrate that the optimized segments exhibit improved radial symmetry when forming a kaleidoscopic disc, leading to significantly greater effectiveness and stability in disrupting various camera pose estimation models compared to the non-optimized KBA_{nat} . In summary, our contributions are as follows:

- Inspired by the prevalent symmetry in nature, we propose a method to construct adversarial kaleidoscopic background with multi-fold radial symmetry in object-centric scenes to effectively disrupt camera pose estimation.
- We optimize the kaleidoscopic background using orientation consistency loss to significantly enhance the attack effectiveness in both the digital and physical worlds.
- To the best of our knowledge, we are the first to utilize background textures as adversarial examples to attack sparse-view camera pose estimation models. Our work introduces a method for constructing challenging samples, which can facilitate improvement in both the performance and robustness of these models in the future.

2. Method

In this section, we first introduce the construction of the multi-fold symmetric kaleidoscopic background, which serves as the foundation of our approach. Leveraging this construction, using natural textures as segments can also generate considerable interference effects on various mod-

els. To enhance the effectiveness of perturbations, we select DUST3R [35], a model capable of performing various 3D tasks that has garnered widespread attention from the research community, as our target for white-box adversarial attacks. We will introduce how to use the proposed projected orientation consistency loss to constrain the camera orientations from any two viewpoints, thereby optimizing the segments to construct a radially symmetric background.

2.1. Kaleidoscopic Background Construction

Unlike conventional adversarial attacks that use a single image as the adversarial example, we construct an adversarial background disc $I_d \in \mathbb{R}^{2\rho \times 2\rho \times 3}$ with a radius ρ from N segment images. To achieve this, we begin by initializing a segment image $I_s \in \mathbb{R}^{w \times h \times 3}$, as shown in Fig. 2(a), with height h , width w , and segment angle θ computed using Eq. 1, where $\lceil \cdot \rceil$ denotes the ceiling function.

$$\theta = \frac{2\pi}{N}, \quad h = \rho, \quad w = \lceil 2\rho \sin \frac{\theta}{2} \rceil \quad (1)$$

For an arbitrary segment of I_d , the corresponding region can be obtained by projecting the image I_s via perspective projection. In this process, solving the perspective projection matrix for mapping the $x'O'y'$ coordinate system to xOy reduces to determining the vertices of the rectangular regions $A'B'C'D'$ and $A_nB_nC_nD_n$ with the help of the OpenCV [4] library. Given the height h and width w of I_s , $\{A', B', C', D'\}$ can be easily calculated as shown in Eq. 2.

$$\{(-\frac{h}{2}, -\frac{w}{2}), (\frac{h}{2}, -\frac{w}{2}), (\frac{h}{2}, \frac{w}{2}), (-\frac{h}{2}, \frac{w}{2})\} \quad (2)$$

As for the n -th rectangle $A_nB_nC_nD_n$, it can be derived by rotating $A_0B_0C_0D_0$ around the origin O by an angle of $n\theta$. Consequently, vertices A_n and B_n lie on a circle with radius ρ_1 , while C_n and D_n lie on a circle with radius ρ_2 , where ρ_1 and ρ_2 are given by Eq. 3.

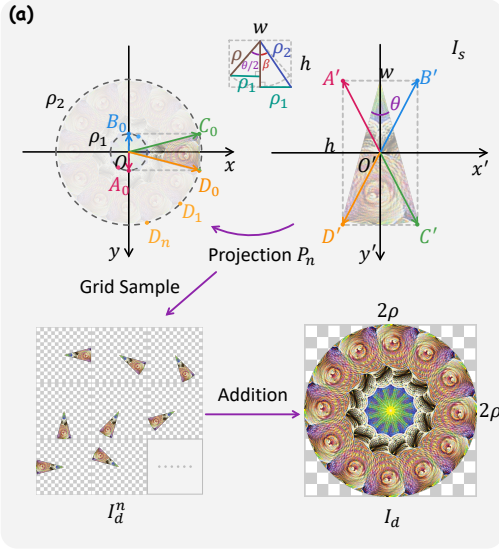
$$\rho_1 = \rho \sin \frac{\theta}{2}, \quad \rho_2 = \sqrt{\rho_1^2 + \rho^2} \quad (3)$$

The coordinates of vertices $A_nB_nC_nD_n$ can further be expressed using Eq. 4, where $\beta = \arctan(\rho_1/\rho)$.

$$\begin{cases} A_n = (\rho_1 \cos(n\theta + \frac{\pi}{2}), \rho_1 \sin(n\theta + \frac{\pi}{2})) \\ B_n = (\rho_1 \cos(n\theta - \frac{\pi}{2}), \rho_1 \sin(n\theta - \frac{\pi}{2})) \\ C_n = (\rho_2 \cos(n\theta - \beta), \rho_2 \sin(n\theta - \beta)) \\ D_n = (\rho_2 \cos(n\theta + \beta), \rho_2 \sin(n\theta + \beta)) \end{cases} \quad (4)$$

By combining Eq. 2 and Eq. 4, the transformation matrix P_n that maps any point in $A'B'C'D'$ to $A_nB_nC_nD_n$ can be easily obtained by calling the `getPerspectiveTransform` function in OpenCV. The projected image $I_d^n \in \mathbb{R}^{2\rho \times 2\rho \times 3}$, obtained by applying P_n to the segment image I_s , can be derived from Eq. 5,

Kaleidoscopic Background Construction



Pose Orientation Consistency Formulation

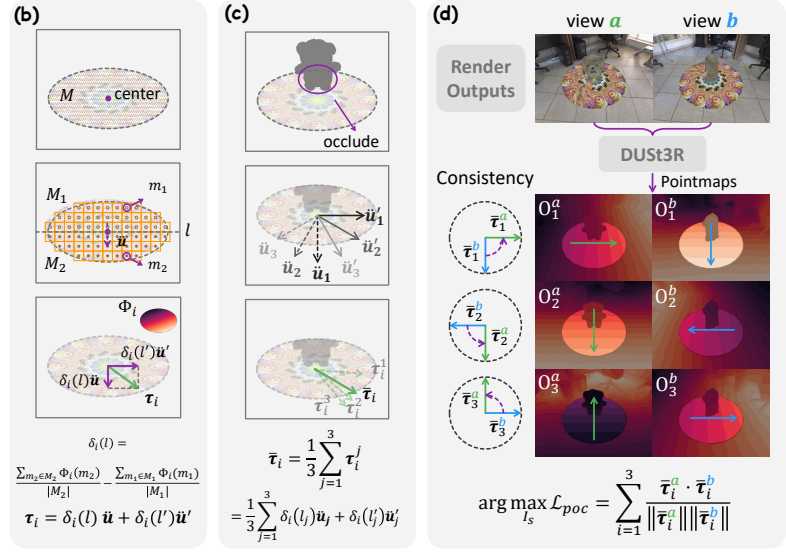


Figure 2. (a) Construction of the kaleidoscopic background disc. (b) Estimation of coordinate flow direction. (c) Calculation of average flow directions across multiple bisections. (d) Computation of the projected orientation consistency loss for camera pose estimation.

where $\mathcal{G}(I_d)$ represents the grid of the image I_d , and each element in $P_n^{-1}\mathcal{G}(I_d) \in \mathbb{R}^{2\rho \times 2\rho \times 3}$ denotes a sampling coordinate from I_s . $G(\cdot)$ can be implemented using the `grid_sample` function in the PyTorch [2] library.

$$I_d^n = G(I_s, P_n^{-1}\mathcal{G}(I_d)) \quad (5)$$

Finally, the kaleidoscopic background image I_d can be generated by performing element-wise addition on the N projected images, as shown in Eq. 6.

$$I_d = \sum_{n=0}^{N-1} I_d^n \quad (6)$$

In fact, a kaleidoscopic background I_d composed of segments of natural texture is already capable of attacking the pose estimation models. However, further optimizing I_d can enhance the attack effectiveness. In the following section, we will introduce the design and physical meaning of the proposed optimization loss.

2.2. Enforced Orientation Consistency Loss

Ideal enforced orientation consistency loss. The camera pose is typically represented by a rotation matrix $R \in \mathbb{R}^{3 \times 3}$ for the camera orientation and a translation vector $T \in \mathbb{R}^{3 \times 1}$ for the position, as shown in Eq. 7 and Eq. 8. Vectors $\mathbf{r}_1, \mathbf{r}_2$, and \mathbf{r}_3 in $\mathbb{R}^{3 \times 1}$, formed by the rows of R , represent the directions of the camera coordinate system axes.

$$R = \begin{bmatrix} r_{11} & r_{21} & r_{31} \\ r_{12} & r_{22} & r_{32} \\ r_{13} & r_{23} & r_{33} \end{bmatrix}^\top = [\mathbf{r}_1 \ \mathbf{r}_2 \ \mathbf{r}_3]^\top \quad (7)$$

$$T = [t_1 \ t_2 \ t_3]^\top \quad (8)$$

For pose estimation models that directly output the matrix R , an ideal attack can be achieved by maximizing the sum of cosine similarities between the corresponding vectors \mathbf{r}_i from two views a and b , as detailed in Eq. 9. Here, $\|\cdot\|$ denotes the L_2 norm of a vector. **Such an attack aims to enforce the convergence of pose orientations from different views to a single direction.** Thereby, a multi-view imaging system degrades into a single-view system in a sense. Such degradation will significantly impact downstream tasks by disrupting the restoration of spatial information.

$$\mathcal{L}_{oc} = \sum_{i=1}^3 \frac{\mathbf{r}_i^a \cdot \mathbf{r}_i^b}{\|\mathbf{r}_i^a\| \|\mathbf{r}_i^b\|} \quad (9)$$

However, recent models such as DUST3R [35] and MAST3R [24] output pointmaps instead of R matrix, leading to the difficulty in directly applying Eq. 9. We define a point in the world, camera, and pixel coordinate systems as (x, y, z) , $(\tilde{x}, \tilde{y}, \tilde{z})$, and (\ddot{x}, \ddot{y}) , respectively. A pointmap $O \in \mathbb{R}^{H \times W \times 3}$ is defined as $H \times W$ points in the camera coordinate system, as shown in Eq. 10, where $\Phi: \mathbb{R}^2 \rightarrow \mathbb{R}^3$ maps (\ddot{x}, \ddot{y}) to $(\tilde{x}, \tilde{y}, \tilde{z})$, H and W represent the spatial size of the pointmap.

$$O = \{\Phi(\ddot{x}, \ddot{y}) \mid \ddot{x} = \{0, \dots, W-1\}, \ddot{y} = \{0, \dots, H-1\}\} \quad (10)$$

The DUST3R model takes a pair of $H \times W \times 3$ images from viewpoints a and b as inputs and simultaneously regresses the pointmaps O^a and O^b in the camera coordinate

system of a . Then, a global alignment strategy is applied to iteratively merge all pointmaps into the same coordinate system and estimate the camera poses for the corresponding images. **While it is possible to obtain \mathbf{r}_i required in Eq. 9, optimizing the adversarial example through backpropagation becomes extremely challenging when applied to such an iterative alignment process.** Therefore, in the following, we will propose an alternative attack strategy that directly enforces orientation consistency based on the pointmaps.

Enforced projected orientation consistency loss. We define the i -th component of Φ by Φ_i , as is illustrated in Eq. 11. The i -th channel of the pointmap O , denoted as $O_i \in \mathbb{R}^{H \times W}$, is then given by Eq. 12.

$$\dot{x} = \Phi_1(\ddot{x}, \ddot{y}), \dot{y} = \Phi_2(\ddot{x}, \ddot{y}), \dot{z} = \Phi_3(\ddot{x}, \ddot{y}) \quad (11)$$

$$O_i = \{\Phi_i(\ddot{x}, \ddot{y}) \mid \ddot{x} = \{0, \dots, W-1\}, \ddot{y} = \{0, \dots, H-1\}\} \quad (12)$$

Note that we only need to consider the part of the pointmap inside the disc region of the kaleidoscopic background. Taking the O_i from an arbitrary viewpoint as an example, the pixel coordinates of all points within the disc region in O_i are defined as a set M . A line l inside the disc passing through the center of the disc region divides M into two parts, M_1 and M_2 , as illustrated in Fig. 2(b). Define the coordinate variation $\delta_i(l)$ between M_1 and M_2 as Eq. 13, where $|\cdot|$ denotes the number of elements in a set. Similarly, for a line l' inside the disc which is perpendicular to l , we can similarly compute its coordinate variation $\delta_i(l')$.

$$\delta_i(l) = \frac{\sum_{m_2 \in M_2} \Phi_i(m_2)}{|M_2|} - \frac{\sum_{m_1 \in M_1} \Phi_i(m_1)}{|M_1|} \quad (13)$$

We define the direction of the coordinate flow $\tau_i \in \mathbb{R}^2$ in Eq. 14, where $\ddot{\mathbf{u}} \in \mathbb{R}^2$ is the unit normal vector of l inside the disc pointing from M_1 to M_2 , and $\ddot{\mathbf{u}}'$ is the counterpart normal vector of l' .

$$\tau_i = \delta_i(l)\ddot{\mathbf{u}} + \delta_i(l')\ddot{\mathbf{u}}' \quad (14)$$

To account for potential occlusions on the disc, three different lines inside the disc $l_j (j = 1, 2, 3)$ are used to estimate coordinate variations from multiple directions, as illustrated in Fig. 2(c). The angle between l_j and l_{j+1} is set to 30 degrees. The average flow direction $\bar{\tau}_i$ is then computed using Eq. 15.

$$\bar{\tau}_i = \frac{1}{3} \sum_{j=1}^3 (\delta_i(l_j)\ddot{\mathbf{u}}_j + \delta_i(l'_j)\ddot{\mathbf{u}}'_j) \quad (15)$$

For two different views a and b , the projected orientation consistency loss \mathcal{L}_{poc} is defined as the sum of the cosine similarities between their average flow directions $\bar{\tau}_i$, as shown in Eq. 16.

$$\mathcal{L}_{poc} = \sum_{i=1}^3 \frac{\bar{\tau}_i^a \cdot \bar{\tau}_i^b}{\|\bar{\tau}_i^a\| \|\bar{\tau}_i^b\|} \quad (16)$$

We visualize the pointmaps O_i^a and O_i^b using heatmaps as shown in Fig. 2(d), where brighter areas indicate larger coordinate values in the camera coordinate system. For a pointmap O_i of a given viewpoint, it can be observed that the coordinates on the disc increase approximately in a single direction, as indicated by the green and blue arrows in Fig. 2(d). In fact, the aforementioned $\bar{\tau}_i$ can be regarded as a mathematical measure of such a flow direction of the coordinates. It is evident that $\bar{\tau}_i$ is highly correlated with the corresponding camera orientation. Intuitively, when the cosine similarity between $\bar{\tau}_i^a$ and $\bar{\tau}_i^b$ are maximized, the camera orientations of views a and b tends to be estimated as identical. Therefore, we maximize the loss function \mathcal{L}_{poc} in Eq. 16 for any two views a and b to realize adversarial attacks against the pose estimation. **Notably, region partitioning can be directly achieved using several pre-designed masks.** Moreover, the loss function \mathcal{L}_{poc} in Eq. 16 is simple to implement and can benefit from parallel computation to significantly enhance efficiency.

Interpretation of \mathcal{L}_{poc} . We hereby interpret the relationship between \mathcal{L}_{poc} and the camera orientation vectors. Following the RDF (right-down-forward) convention [4], we suppose that the kaleidoscopic background lies on the plane $C : y = 0$ in the world coordinate system. We denote the projection of the camera orientation vector \mathbf{r}_i onto plane C as $\hat{\mathbf{r}}_i$ in Eq. 17, where $\mathbf{c} = (0, -1, 0)^\top$ is the normal vector of plane C and $i = 1, 2, 3$.

$$\hat{\mathbf{r}}_i = \mathbf{r}_i - (\mathbf{r}_i \cdot \mathbf{c})\mathbf{c} = [r_{i1} \ 0 \ r_{i3}]^\top \quad (17)$$

We define the mapping from the world coordinate system to the camera coordinate system as $\tilde{\Phi} : \mathbb{R}^3 \rightarrow \mathbb{R}^3$ in Eq. 18. Similar to Eq. 11, $\tilde{\Phi}_i : \mathbb{R}^3 \rightarrow \mathbb{R}^1$ is defined as the i -th component of $\tilde{\Phi}$.

$$\begin{bmatrix} \dot{x} \\ \dot{y} \\ \dot{z} \end{bmatrix} = \tilde{\Phi} \begin{bmatrix} x \\ y \\ z \end{bmatrix} = R \begin{bmatrix} x \\ y \\ z \end{bmatrix} + T \quad (18)$$

The Jacobian matrix $J_{\tilde{\Phi}}$ of the mapping $\tilde{\Phi}$ can be calculated using Eq. 19, where $\nabla \tilde{\Phi}_i$ represents the gradient of the i -th coordinate in the camera coordinate system with respect to the x , y , and z . Combining Eq. 7 and Eq. 19, it is evident that $\nabla \tilde{\Phi}_i = \mathbf{r}_i$.

$$J_{\tilde{\Phi}} = R = \begin{bmatrix} r_{11} & r_{12} & r_{13} \\ r_{21} & r_{22} & r_{23} \\ r_{31} & r_{32} & r_{33} \end{bmatrix} = [\nabla \tilde{\Phi}_1 \ \nabla \tilde{\Phi}_2 \ \nabla \tilde{\Phi}_3]^\top \quad (19)$$

In the world coordinate system, let L be the line within plane C , of which the imaging result is line l used in Eq. 13. Physically, L divides the kaleidoscopic background disc evenly into two halves. As a result, the value of $\delta_i(l)$ computed by Eq. 13 can be interpreted as the difference $\tilde{\Phi}_i(s_2) - \tilde{\Phi}_i(s_1)$, where s_2 and s_1 are the centroids of the

Algorithm 1 Kaleidoscopic Background Optimization

Input: Victim model DUST3R $f(\cdot, \cdot)$, differentiable renderer with augmentations $R(\cdot, \cdot, \cdot, \cdot)$, 3D objects O , environments E , disc object o_d , maximum number of optimization iterations T , color-set clipping frequency T_c

Output: Kaleidoscopic segment image I_s

- 1: Initialize I_s^0 with uniform random noise;
 - 2: **for** $t = 0$ to T **do**
 - 3: Construct the texture I_d for o_d from I_s^t using Eq. 6;
 - 4: Randomly select $o \in O$ and $e \in E$;
 - 5: Render two images I_a and I_b from random viewpoints using $R(o, e, o_d, I_s^0)$ with augmentations;
 - 6: Extract Pointmaps $f(I_a, I_b)$ from DUST3R;
 - 7: Compute orientation consistency loss using Eq. 16;
 - 8: Update I_s^{t+1} using Eq. 23;
 - 9: **if** $t \bmod T_c = 0$ **then**
 - 10: Clip colors in I_s^{t+1} to the CMYK color space;
 - 11: **end if**
 - 12: **end for**
 - 13: **return** I_s^T
-

two halves of the disc. Suppose $\mathbf{u} \in \mathbb{R}^3$ is the unit normal vector of L inside the disc, the gradient of $\tilde{\Phi}_i$ along the direction of \mathbf{u} can be expressed using Eq. 20, where $\|s_1 - s_2\|$ represents the distance between s_1 and s_2 . Similarly, we can define line L' and $\mathbf{u}' \in \mathbb{R}^3$ and calculate the gradient of $\tilde{\Phi}_i$ along the direction of \mathbf{u}' as $\nabla_{\mathbf{u}'}$. As such, the gradient of $\tilde{\Phi}_i$ in plane C can be expressed by Eq. 21.

$$\nabla_{\mathbf{u}} = \frac{\tilde{\Phi}_i(s_2) - \tilde{\Phi}_i(s_1)}{\|s_1 - s_2\|} = \frac{\delta_i(l)}{\|s_1 - s_2\|} \quad (20)$$

$$\hat{\nabla} \tilde{\Phi}_i = \nabla_{\mathbf{u}} \mathbf{u} + \nabla_{\mathbf{u}'} \mathbf{u}' = \frac{\delta_i(l) \mathbf{u} + \delta_i(l') \mathbf{u}'}{\|s_1 - s_2\|} \approx \hat{\mathbf{r}}_i \quad (21)$$

In fact, $\hat{\nabla} \tilde{\Phi}_i$ can be regarded as an estimation of the projection of $\nabla \tilde{\Phi}_i$ onto plane C since vectors \mathbf{u} and \mathbf{u}' are defined within the plane, namely $\hat{\mathbf{r}}_i$. By assuming orthogonal projection as well as considering the symmetry of the disc, the cosine similarity between $\tilde{\tau}_i^a$ and $\tilde{\tau}_i^b$ in Eq. 16 can be used as a fair approximation of the cosine similarity between $\hat{\mathbf{r}}_i^a$ and $\hat{\mathbf{r}}_i^b$. Maximizing \mathcal{L}_{poc} is approximately equivalent to maximizing the sum of cosine similarities of the projected camera orientation vectors $\hat{\mathbf{r}}_i$ between different poses, as shown in Eq. 22.

$$\arg \max_{I_s} \mathcal{L}_{poc} \Leftrightarrow \arg \max_{I_s} \sum_{i=1}^3 \frac{\hat{\mathbf{r}}_i^a \cdot \hat{\mathbf{r}}_i^b}{\|\hat{\mathbf{r}}_i^a\| \|\hat{\mathbf{r}}_i^b\|} \quad (22)$$

In fact, \mathcal{L}_{poc} can be regarded as a relaxed version of \mathcal{L}_{oc} by only enforcing camera orientation consistency in the projected plane. Nevertheless, experiments demonstrate that \mathcal{L}_{poc} achieves a satisfactory attacking effect in practice.

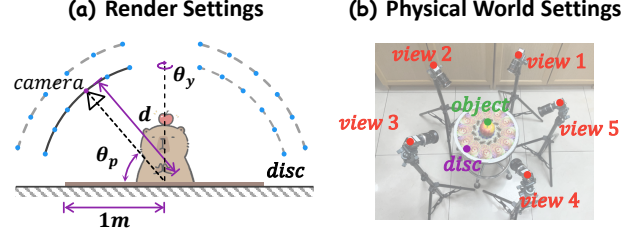


Figure 3. (a) The setup for rendering scenes in the digital world. (b) The setup for testing scenes in the physical world.

2.3. The Overall Optimization Process

The overall optimization of the kaleidoscopic patterns background is illustrated in Algorithm 1. We render two images from different viewpoints each time, applying various data augmentation techniques. For optimization, we maximize the loss computed in Eq. 16 and update the kaleidoscopic segment image I_s as described in Eq. 23. Here, $\alpha = 1/255$ serves as the step size, $\text{sign}(\cdot)$ indicates the sign function, and $\text{clip}_{\{0,1\}}(\cdot)$ constrains values within the $[0,1]$ range.

$$I_s^{t+1} = \text{clip}_{\{0,1\}}(I_s^t + \alpha \cdot \text{sign}(\nabla_{I_s} \mathcal{L}_{poc})) \quad (23)$$

To improve the physical-world feasibility of the kaleidoscopic background, we clip RGB values to the CMYK color space after a specified number of optimization steps. Refer to the supplementary material for further details.

3. Experiments

To validate the effectiveness of our approach, we perform a series of experiments in both the digital and physical worlds. In the digital world, we focus on optimizing adversarial backgrounds and conducting ablation studies. In contrast, the physical world experiments primarily evaluate the effectiveness and generalizability of our approach in attacking various camera pose estimation models under complex real-world scenarios. For these experiments, **Nature** refers to a desktop texture, with its radially symmetric version denoted as **KBA_{nat}** and its optimized counterpart as **KBA_{opt}**. We use consistent evaluation metrics across both types of experiments for a comprehensive comparison.

Evaluation metrics. Following [24, 26, 34, 35, 44], we evaluated the accuracy of pose estimation using Relative Rotation Accuracy (RRA), Relative Translation Accuracy (RTA), and mean Average Accuracy (mAA). Specifically, RRA compares the relative rotation $R_i R_j^T$ from the i -th to the j -th camera with the ground truth $R_i^* R_j^{*\top}$, while RTA measures the angle between the predicted vector T_{ij} and the ground truth vector T_{ij}^* pointing from camera i to camera j . We report $\text{RTA}@ \gamma$ and $\text{RRA}@ \gamma$ ($\gamma \in \{5, 15, 30\}$), representing the percentage of camera pairs with RRA or RTA values below the threshold γ . Furthermore, we compute the

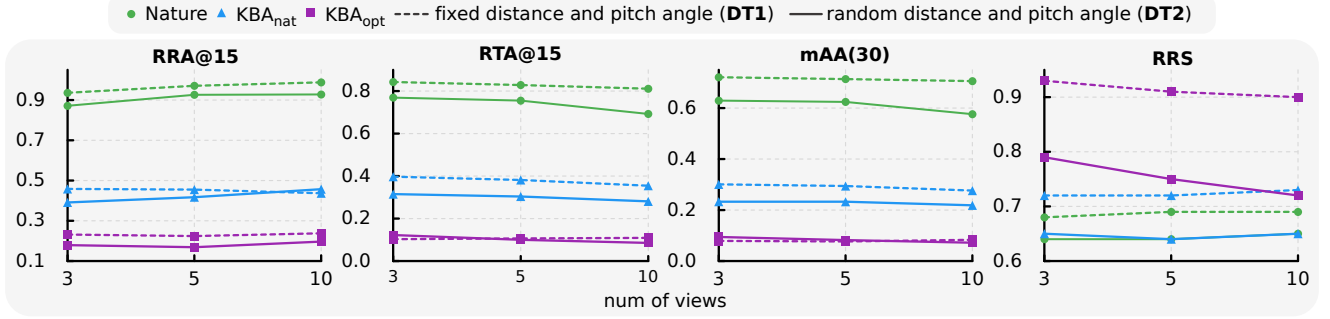


Figure 4. Experimental results of attacking DUST3R in the digital world with various background discs and view counts. Lower values of RRA@15, RTA@15, and mAA(30), along with higher RRS values, signify better performance against adversarial attacks.

Methods	Textures	RRA@5 ↓	RRA@15 ↓	RRA@30 ↓	RTA@5 ↓	RTA@15 ↓	RTA@30 ↓	mAA(30) ↓	RRS ↑
DUST3R	Nature	1.00 ±0.02	1.00 ±0.00	1.00 ±0.00	0.98 ±0.03	1.00 ±0.00	1.00 ±0.00	0.95 ±0.01	0.62 ±0.01
	KBA _{nat}	0.30 ±0.19	0.32 ±0.20	0.36 ±0.20	0.31 ±0.19	0.37 ±0.19	0.46 ±0.19	0.31 ±0.19	0.77 ±0.08
	KBA _{opt}	0.00 ±0.00	0.00 ±0.00	0.00 ±0.01	0.00 ±0.01	0.02 ±0.03	0.09 ±0.04	0.00 ±0.00	0.94 ±0.02
MASt3R	Nature	0.35 ±0.10	0.99 ±0.01	1.00 ±0.00	0.78 ±0.09	1.00 ±0.01	1.00 ±0.00	0.80 ±0.02	0.62 ±0.00
	KBA _{nat}	0.14 ±0.10	0.45 ±0.19	0.51 ±0.20	0.32 ±0.16	0.51 ±0.19	0.63 ±0.20	0.36 ±0.15	0.72 ±0.08
	KBA _{opt}	0.02 ±0.04	0.06 ±0.10	0.07 ±0.10	0.05 ±0.08	0.12 ±0.09	0.22 ±0.08	0.05 ±0.08	0.86 ±0.05
Ray Diffusion	Nature	0.06 ±0.05	0.79 ±0.08	0.99 ±0.02	0.33 ±0.08	0.96 ±0.04	0.99 ±0.02	0.61 ±0.04	0.62 ±0.01
	KBA _{nat}	0.01 ±0.02	0.29 ±0.11	0.62 ±0.17	0.10 ±0.06	0.51 ±0.16	0.76 ±0.14	0.28 ±0.10	0.62 ±0.02
	KBA _{opt}	0.00 ±0.01	0.06 ±0.05	0.21 ±0.10	0.02 ±0.02	0.17 ±0.10	0.39 ±0.12	0.07 ±0.05	0.69 ±0.05
Ray Regression	Nature	0.06 ±0.05	0.79 ±0.09	0.97 ±0.04	0.26 ±0.10	0.90 ±0.07	0.97 ±0.04	0.60 ±0.05	0.62 ±0.01
	KBA _{nat}	0.01 ±0.02	0.27 ±0.11	0.59 ±0.16	0.08 ±0.04	0.49 ±0.15	0.70 ±0.13	0.26 ±0.09	0.62 ±0.02
	KBA _{opt}	0.00 ±0.00	0.10 ±0.07	0.35 ±0.16	0.03 ±0.02	0.26 ±0.12	0.49 ±0.14	0.11 ±0.06	0.66 ±0.06
RelPose++	Nature	0.33 ±0.11	0.57 ±0.10	0.57 ±0.10	0.25 ±0.09	0.52 ±0.10	0.57 ±0.10	0.43 ±0.08	0.62 ±0.01
	KBA _{nat}	0.06 ±0.04	0.30 ±0.10	0.46 ±0.12	0.10 ±0.05	0.40 ±0.13	0.55 ±0.11	0.25 ±0.08	0.61 ±0.01
	KBA _{opt}	0.04 ±0.04	0.20 ±0.08	0.30 ±0.09	0.08 ±0.04	0.27 ±0.10	0.39 ±0.10	0.17 ±0.07	0.66 ±0.05
PoseDiffusion	Nature	0.39 ±0.11	0.64 ±0.10	0.65 ±0.10	0.41 ±0.11	0.61 ±0.11	0.64 ±0.10	0.51 ±0.09	0.62 ±0.00
	KBA _{nat}	0.02 ±0.02	0.19 ±0.06	0.40 ±0.10	0.10 ±0.04	0.42 ±0.10	0.61 ±0.11	0.19 ±0.05	0.62 ±0.03
	KBA _{opt}	0.02 ±0.02	0.14 ±0.06	0.26 ±0.12	0.04 ±0.03	0.23 ±0.11	0.40 ±0.12	0.11 ±0.06	0.65 ±0.05

Table 1. Experimental results of attacking various camera pose estimation models with different background discs in the physical world. Each cell contains two values: the larger value represents the mean of the metric across all samples, while the smaller value indicates the standard deviation of the metric across different object categories. Bold values indicate the best performance of adversarial attacks.

mAA(30), which is defined as the area under the accuracy curve of angular differences at $\min(\text{RRA}@30, \text{RTA}@30)$. Beyond these three standard metrics, we introduce a custom Relative Rotation Similarity (RRS) metric, leveraging cosine similarity to assess the similarity between different predicted relative rotations $R_i R_j^\top$. An RRS value close to 1 signifies high consistency in pose orientations.

3.1. Experiments in the Digital World

In this section, we first introduce the data used for adversarial attacks, followed by the test setup in the digital world. Finally, we present the camera pose estimation results un-

der different backgrounds for 3, 5, and 10 views.

Attack data and parameters. We use six HDRI images of indoor and outdoor scenes from Polyhaven [16], each mapped onto a spherical mesh to create realistic backgrounds. Additionally, we select 32 3D objects from 20 categories in OmniObject3D [40] for adversarial attacks. Both KBA_{nat} and KBA_{opt} are constructed with $N = 12$ segments. At each optimization step, objects and backgrounds are randomly selected to construct the scene.

Test setups. For the test, we additionally select 10 HDRI images from Polyhaven and 25 objects spanning 25 categories in the OmniObject3D dataset, none of which are in-

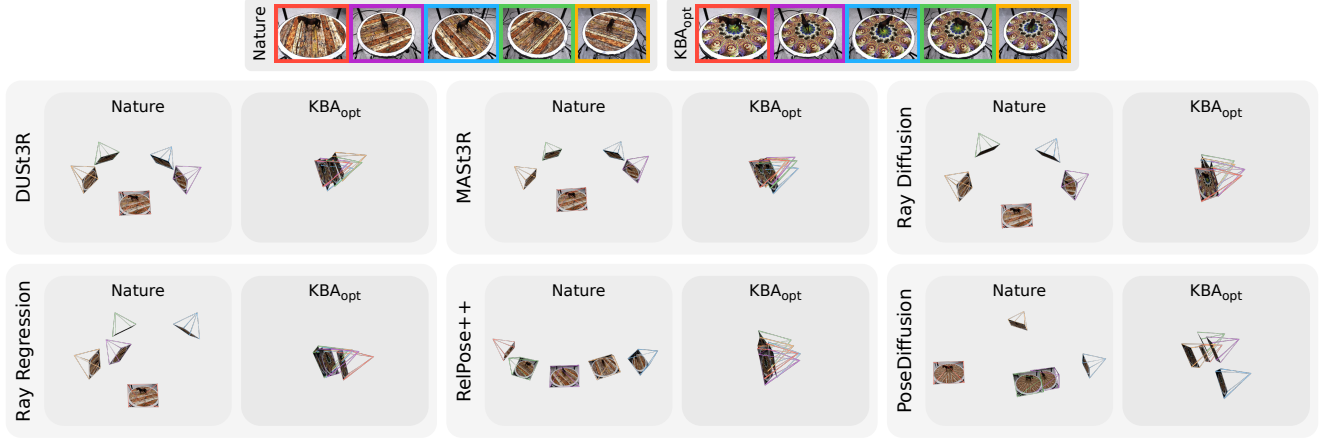


Figure 5. Visualization of experimental results for discs with varying backgrounds across different camera pose estimation models in the physical world. The color of the image borders corresponds to the color of the associated pose pyramid.

cluded in the attack data. The rendered scene, depicted in Fig. 3(a), includes a 3D object, background disc, and environment, with the disc radius set to 1 m, objects centered and scaled within a $0.8 \times 0.8 \times 0.8$ m bounding box, and the rendering camera positioned at distance d facing the disc center, with pitch angle θ_p and yaw angle θ_y defining its orientation. In order to increase the diversity of experiments and the generalization of results, we configured $6 \times 36 \times 6 = 1296$ parameter combinations using six pitch angles (ranging from 10° to 85°), 36 yaw angles (in increments of 10°), and six distances (ranging from 2.0 m to 3.0 m). Images and masks for the 3D objects, discs, and environments were rendered and combined during testing to produce the final image. We design two testing scenarios, **DT1** and **DT2**, to assess the impact of different background discs on camera pose estimation. In **DT1**, the pitch angle is fixed at 55° and the distance at 2.4 m, while varying the yaw angles. In **DT2**, 1296 camera poses are randomly selected for a more comprehensive evaluation. Each scenario includes four samples per object-environment combination, resulting in a total of $25 \times 10 \times 4 = 1000$ samples.

Experimental results. The results in Fig. 4 demonstrate that KBA_{nat} is already capable of significantly reducing the RRA, RTA, and mAA metrics compared to the natural background. KBA_{opt} obtains radially symmetric textures through optimization, showing a marked improvement in attack effectiveness compared to KBA_{nat} . It is noteworthy that, although our adversarial attack optimization process is conducted on a pair of images from two views, stable adversarial attack effectiveness is observed when using 3, 5, or 10 images for camera pose estimation, regardless of whether in the same longitude DT1 or the more random DT2 settings. Regarding the RRS metric, both KBA_{nat} and KBA_{opt} enhance camera orientation similarity in DT1 with yaw angle changes, with KBA_{opt} achieving a similarity close to 0.9.

Although enforcing identical camera orientations across all views becomes challenging as the number of images increases in the DT2 setting, our method still significantly disrupts camera pose estimation, as indicated by the RRA, RTA, and mAA metrics. We also conduct adversarial transferability experiments in the digital world. The results show that the radially symmetric textures optimized by KBA_{opt} exhibit strong transferability across various models. The details are provided in the supplementary material.

3.2. Experiments in the Physical World

In this section, we first describe the physical-world test setup, followed by a detailed analysis of the results obtained with various background textures across multiple models. Additionally, we present visualizations of the camera pose estimation outcomes based on a set of captured images, further illustrating the effectiveness of our approach.

Test setups. We selected 24 different 3D objects, including vegetables, fruits, animals, and vehicles. To ensure complete capture of the disc while maintaining good imaging quality for the objects, we crafted two discs: one with a radius of 15 cm for objects ranging from 10 to 20 cm, and another with a radius of 20 cm for objects ranging from 20 to 30 cm. As shown in Fig. 3(b), five industrial cameras are evenly distributed around the disc, with their lenses directed toward the center at distances ranging from 20 to 50 cm. Under normal indoor lighting conditions, we calibrated the cameras using a calibration board and simultaneously captured object-centric images from five different viewpoints. We captured five groups of images for each object, adjusting the camera poses between groups to ensure data diversity.

Experimental results. We evaluated the pose estimation performance of Nature, KBA_{nat} , and KBA_{opt} in the physical world, across both the white-box model DUST3R [35] and the black-box models MAST3R [24], Ray-

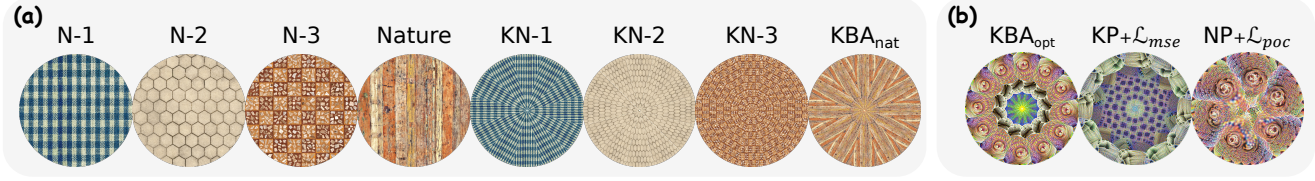


Figure 6. (a) Naturally symmetrical textures found in nature (denoted as N-1,2,3) and unoptimized radially symmetrical textures derived from them (denoted as KN-1,2,3). (b) Textures optimized using different combinations of loss functions and background patterns.

Textures	RRA@15 ↓	RTA@15 ↓	mAA(30) ↓	RRS ↑
N-1	0.89 ±0.02	0.78 ±0.05	0.63 ±0.02	0.64 ±0.01
N-2	0.91 ±0.02	0.78 ±0.07	0.66 ±0.05	0.64 ±0.01
N-3	0.97 ±0.01	0.87 ±0.06	0.78 ±0.05	0.64 ±0.01
Nature	0.97 ±0.01	0.83 ±0.07	0.71 ±0.05	0.64 ±0.01
KN-1	0.70 ±0.04	0.58 ±0.05	0.45 ±0.02	0.64 ±0.01
KN-2	0.56 ±0.05	0.47 ±0.04	0.38 ±0.03	0.66 ±0.01
KN-3	0.45 ±0.04	0.40 ±0.03	0.32 ±0.02	0.67 ±0.01
KBA _{nat}	0.46 ±0.06	0.38 ±0.03	0.29 ±0.02	0.67 ±0.01
KBA _{opt}	0.22 ±0.07	0.11 ±0.02	0.08 ±0.02	0.86 ±0.01
KP + \mathcal{L}_{mse}	0.27 ±0.12	0.16 ±0.04	0.13 ±0.04	0.76 ±0.03
NP + \mathcal{L}_{poc}	0.59 ±0.08	0.35 ±0.02	0.29 ±0.02	0.70 ±0.01

Table 2. Camera pose estimation results on DUST3R with different backgrounds using the DT1 5 images setting. Bold values indicate the best performance among adversarial attacks.

Diffusion [44], RayRegression [44], PoseDiffusion [34], and RelPose++ [26], as shown in Tab. 1. The experimental results show that KBA_{nat} achieves notable attack effectiveness across various pose estimation models. In comparison, the optimized KBA_{opt} exhibits significantly higher performance with smaller standard deviations across metrics, indicating more consistent adversarial attack effectiveness across various object categories. We visualize the camera pose estimation results of various methods on five images with differing perspectives, where the disks correspond to Nature and KBA_{opt}, as shown in Fig. 5. KBA_{opt} exhibits stable adversarial attack performance and effective transferability across multiple black-box models. Notably, KBA_{opt} maximizes the consistency of pose orientation during the attack without explicitly constraining camera positions. However, physical experiments reveal that KBA_{opt} leads to nearly overlapping camera positions, approximating the situation where five images are captured from a single location, further demonstrating the effectiveness of our adversarial attacks. We further visualize the camera pose estimation results in more complex scenarios, including cases where various objects are placed on a disc, the disc is off-centered in the image, and scene-centric environments, to demonstrate the generalizability of our approach. These vi-

sualizations, along with a discussion on the performance of existing patch defense methods against our attacks, are provided in the supplementary material.

3.3. Additional Ablation Studies

In this section, we validate the effectiveness of the radially symmetric texture pattern and the proposed loss function through ablation studies. We first evaluate several symmetric textures found in nature, including woven fabric, hexagonal tile patterns, and quadrilateral tile patterns, as depicted in Fig. 6 (a). The results on DUST3R in Tab. 2 indicate that such natural symmetry has limited impact on camera pose estimation. Building on these natural textures, we construct the corresponding kaleidoscopic backgrounds, as illustrated by KN-1, KN-2, and KN-3 in Fig. 6 (a). Experiments demonstrate that radially symmetric textures constructed from various natural patterns have already shown significant interference in camera pose estimation. To validate the effectiveness of KBA_{opt} (KP + \mathcal{L}_{poc}), we further test a typical patch-based optimization applied to the entire image (NP) and a simple loss strategy minimizing the output MSE across views (\mathcal{L}_{mse}). The textures obtained from the optimization of different method combinations are shown in Fig. 6 (b). Tab. 2 indicates that combining NP and \mathcal{L}_{mse} with our \mathcal{L}_{poc} and KP reduces the effectiveness of adversarial attacks, further validating the roles of radially symmetric textures and our loss function.

4. Conclusions

In this paper, we propose a method for constructing the multi-fold radial symmetric adversarial kaleidoscopic background that exhibits notable similarity across multiple viewpoints to attack camera pose estimation models. We propose a projected orientation consistency loss for optimizing the kaleidoscopic background based on pointmaps, leading to further improvements in attack effectiveness. Experimental results demonstrate that our approach effectively attacks camera pose estimation models under both white-box and black-box settings in the digital and physical worlds, while maintaining strong robustness across varying scenes and camera configurations.

5. Acknowledgements

This work was supported by the National Natural Science Foundation of China (62376024), the National Science and Technology Major Project (2022ZD0117902), and the Fundamental Research Funds for the Central Universities (FRF-TP-22-043A1).

References

- [1] Sameer Agarwal, Noah Snavely, Ian Simon, Steven M. Seitz, and Richard Szeliski. Building rome in a day. In *Proceedings of IEEE International Conference on Computer Vision (ICCV)*, pages 72–79, 2009. 1
- [2] Jason Ansel, Edward Yang, Horace He, and et al. Pytorch 2: Faster machine learning through dynamic python bytecode transformation and graph compilation. In *Proceedings of the 29th ACM International Conference on Architectural Support for Programming Languages and Operating Systems, Volume 2 (ASPLOS '24)*, 2024. 3
- [3] Philip Ball. *Nature's Patterns: A Tapestry in Three Parts*. Oxford University Press, 2009. 2
- [4] G. Bradski. The opencv library. *Dr. Dobbs's Journal of Software Tools*, 2000. 2, 4
- [5] Tom B Brown, Dandelion Mané, Aurko Roy, Martín Abadi, and Justin Gilmer. Adversarial patch. *arXiv preprint arXiv:1712.09665*, 2017. 1
- [6] Nicholas Carlini and David Wagner. Towards evaluating the robustness of neural networks. In *Proceedings of IEEE Symposium on Security and Privacy (SP)*, pages 39–57, 2017. 1
- [7] Stephen Casper, Max Nadeau, Dylan Hadfield-Menell, and Gabriel Kreiman. Robust feature-level adversaries are interpretability tools. In *Proceedings of Annual Conference on Neural Information Processing Systems (NeurIPS)*, pages 33093–33106, 2022. 1
- [8] Zhaoyu Chen, Bo Li, Shuang Wu, Jianghe Xu, Shouhong Ding, and Wenqiang Zhang. Shape matters: Deformable patch attack. In *Proceedings of European Conference on Computer Vision (ECCV)*, pages 529–548, 2022. 1
- [9] David Crandall, Andrew Owens, Noah Snavely, and Dan Huttenlocher. Discrete-continuous optimization for large-scale structure from motion. In *Proceedings of IEEE/CVF Conference on Computer Vision and Pattern Recognition (CVPR)*, pages 3001–3008, 2011. 1
- [10] Devikalyan Das, Christopher Wewer, Raza Yunus, Eddy Ilg, and Jan Eric Lenssen. Neural parametric gaussians for monocular non-rigid object reconstruction. In *Proceedings of IEEE/CVF Conference on Computer Vision and Pattern Recognition (CVPR)*, pages 10715–10725, 2024. 1
- [11] X. Ding, J. Chen, H. Yu, Y. Shang, Y. Qin, and H. Ma. Transferable adversarial attacks for object detection using object-aware significant feature distortion. In *Proceedings of the AAAI Conference on Artificial Intelligence (AAAI)*, pages 1546–1554, 2024. 1
- [12] Xinlong Ding, Hongwei Yu, Jiansheng Chen, Jinlong Wang, Jintai Du, and Huimin Ma. Invisible pedestrians: Synthesizing adversarial clothing textures to evade industrial camera-based 3d detection. In *Proceedings of International Conference on Multimedia and Expo (ICME)*, pages 1–6, 2024. 1
- [13] Yinpeng Dong, Fangzhou Liao, Tianyu Pang, Hang Su, Jun Zhu, Xiaolin Hu, and Jianguo Li. Boosting adversarial attacks with momentum. In *Proceedings of IEEE/CVF Conference on Computer Vision and Pattern Recognition (CVPR)*, pages 9185–9193, 2018. 1
- [14] Khang Truong Giang, Soohwan Song, and Sungho Jo. Learning to produce semi-dense correspondences for visual localization. In *Proceedings of IEEE/CVF Conference on Computer Vision and Pattern Recognition (CVPR)*, pages 19468–19478, 2024. 1
- [15] Ian J Goodfellow, Jonathon Shlens, and Christian Szegedy. Explaining and harnessing adversarial examples. *arXiv preprint arXiv:1412.6572*, 2014. 1
- [16] Poly Haven. Poly haven: The public 3d asset library. <https://polyhaven.com/>, 2024. 6
- [17] Z. Hu, S. Huang, X. Zhu, F. Sun, B. Zhang, and X. Hu. Adversarial texture for fooling person detectors in the physical world. In *Proceedings of IEEE/CVF Conference on Computer Vision and Pattern Recognition (CVPR)*, pages 13307–13316, 2022. 1
- [18] Hao Huang, Ziyang Chen, Huanran Chen, Yongtao Wang, and Kevin Zhang. T-sea: Transfer-based self-ensemble attack on object detection. In *Proceedings of IEEE/CVF Conference on Computer Vision and Pattern Recognition (CVPR)*, pages 20514–20523, 2023. 1
- [19] Hanwen Jiang, Zhenyu Jiang, Kristen Grauman, and Yuke Zhu. Few-view object reconstruction with unknown categories and camera poses. In *International Conference on 3D Vision (3DV)*, pages 31–41, 2024. 1
- [20] Jiantong Jiang, Zeyi Wen, Atif Mansoor, and Ajmal Mian. Efficient hyperparameter optimization with adaptive fidelity identification. In *Proceedings of IEEE/CVF Conference on Computer Vision and Pattern Recognition (CVPR)*, pages 26181–26190, 2024. 1
- [21] Danny Karmon, Daniel Zoran, and Yoav Goldberg. Lavan: Localized and visible adversarial noise. In *Proceedings of International Conference on Machine Learning (ICML)*, pages 2507–2515, 2018. 1
- [22] Alexey Kurakin, Ian J Goodfellow, and Samy Bengio. Adversarial examples in the physical world. In *Proceedings of International Conference on Learning Representations (ICLR)*, 2017. 1
- [23] Haechan Lee, Wonjoon Jin, Seung-Hwan Baek, and Sunghyun Cho. Generalizable novel-view synthesis using a stereo camera. In *Proceedings of IEEE/CVF Conference on Computer Vision and Pattern Recognition (CVPR)*, pages 4939–4948, 2024. 1
- [24] Vincent Leroy, Yohann Cabon, and Jerome Revaud. Grounding image matching in 3d with mast3r. In *Proceedings of European Conference on Computer Vision (ECCV)*, 2024. 1, 3, 5, 7
- [25] Jiawei Li, Hongwei Yu, Jiansheng Chen, Xinlong Ding, Jinlong Wang, Jinyuan Liu, Bochao Zou, and Huimin Ma. A²net: Adversarial attack resilient network for robust infrared and visible image fusion. In *Proceedings of the AAAI*

- Conference on Artificial Intelligence (AAAI)*, pages 4770–4778, 2025. [1](#)
- [26] Amy Lin, Jason Y Zhang, Deva Ramanan, and Shubham Tulsiani. Relpose++: Recovering 6d poses from sparse-view observations. In *International Conference on 3D Vision (3DV)*, pages 106–115, 2024. [1](#), [5](#), [8](#)
- [27] Zhicheng Lu, Xiang Guo, Le Hui, Tianrui Chen, Min Yang, Xiao Tang, Feng Zhu, and Yuchao Dai. 3d geometry-aware deformable gaussian splatting for dynamic view synthesis. In *Proceedings of IEEE/CVF Conference on Computer Vision and Pattern Recognition (CVPR)*, pages 8900–8910, 2024. [1](#)
- [28] Aleksander Madry, Aleksandar Makelov, Ludwig Schmidt, Dimitris Tsipras, and Adrian Vladu. Towards deep learning models resistant to adversarial attacks. In *Proceedings of International Conference on Learning Representations (ICLR)*, 2017. [1](#)
- [29] Nikhila Ravi, Jeremy Reizenstein, David Novotny, Taylor Gordon, Wan-Yen Lo, Justin Johnson, and Georgia Gkioxari. Accelerating 3d deep learning with pytorch3d. *arXiv preprint arXiv:2007.08501*, 2020. [2](#)
- [30] Chris Rockwell, Justin Johnson, and David F. Fouhey. The 8-point algorithm as an inductive bias for relative pose prediction by vits. In *International Conference on 3D Vision (3DV)*, pages 1–11, 2022. [1](#)
- [31] Frederik Schaffalitzky and Andrew Zisserman. Multi-view matching for unordered image sets, or “how do i organize my holiday snaps?”. In *Proceedings of European Conference on Computer Vision (ECCV)*, pages 414–431, 2002. [1](#)
- [32] Samarth Sinha, Jason Y. Zhang, Andrea Tagliasacchi, Igor Gilitschenski, and David B. Lindell. Sparsepose: Sparse-view camera pose regression and refinement. In *Proceedings of IEEE/CVF Conference on Computer Vision and Pattern Recognition (CVPR)*, pages 21349–21359, 2023. [1](#)
- [33] Christian Szegedy, Wojciech Zaremba, Ilya Sutskever, Joan Bruna, Dumitru Erhan, Ian Goodfellow, and Rob Fergus. Intriguing properties of neural networks. In *Proceedings of International Conference on Learning Representations (ICLR)*, 2014. [1](#)
- [34] Jianyuan Wang, Christian Rupprecht, and David Novotny. Posediffusion: Solving pose estimation via diffusion-aided bundle adjustment. In *Proceedings of IEEE International Conference on Computer Vision (ICCV)*, pages 9773–9783, 2023. [1](#), [5](#), [8](#)
- [35] Shuzhe Wang, Vincent Leroy, Yohann Cabon, Boris Chidlovskii, and Jerome Revaud. Dust3r: Geometric 3d vision made easy. In *Proceedings of IEEE/CVF Conference on Computer Vision and Pattern Recognition (CVPR)*, pages 20697–20709, 2024. [1](#), [2](#), [3](#), [5](#), [7](#)
- [36] Xingxing Wei, Ying Guo, Jie Yu, and Bo Zhang. Simultaneously optimizing perturbations and positions for black-box adversarial patch attacks. *IEEE Transactions on Pattern Analysis and Machine Intelligence*, 45(7):9041–9054, 2023. [1](#)
- [37] X. Wei, J. Yu, and Y. Huang. Physically adversarial infrared patches with learnable shapes and locations. In *Proceedings of IEEE/CVF Conference on Computer Vision and Pattern Recognition (CVPR)*, pages 12334–12342, 2023. [1](#)
- [38] Kyle Wilson and Noah Snavely. Robust global translations with 1dsfm. In *Proceedings of European Conference on Computer Vision (ECCV)*, pages 61–75, 2014. [1](#)
- [39] Tong Wu, Xuefei Ning, Wenshuo Li, Ranran Huang, Huazhong Yang, and Yu Wang. Physical adversarial attack on vehicle detector in the carla simulator. *arXiv preprint arXiv:2007.16118*, 2020. [1](#)
- [40] Tong Wu, Jiarui Zhang, Xiao Fu, Yuxin Wang, Jiawei Ren, Liang Pan, Wayne Wu, Lei Yang, Jiaqi Wang, Chen Qian, Dahua Lin, and Ziwei Liu. Omniobject3d: Large-vocabulary 3d object dataset for realistic perception, reconstruction and generation. In *Proceedings of IEEE/CVF Conference on Computer Vision and Pattern Recognition (CVPR)*, 2023. [6](#)
- [41] Desai Xie, Jiahao Li, Hao Tan, Xin Sun, Zhixin Shu, Yi Zhou, Sai Bi, Sören Pirk, and Arie E. Kaufman. Carve3d: Improving multi-view reconstruction consistency for diffusion models with rl finetuning. In *Proceedings of IEEE/CVF Conference on Computer Vision and Pattern Recognition (CVPR)*, pages 6369–6379, 2024. [1](#)
- [42] H. Yu, J. Chen, X. Ding, Y. Zhang, T. Tang, and H. Ma. Step vulnerability guided mean fluctuation adversarial attack against conditional diffusion models. In *Proceedings of the AAAI Conference on Artificial Intelligence (AAAI)*, pages 6791–6799, 2024. [1](#)
- [43] Jason Y. Zhang, Deva Ramanan, and Shubham Tulsiani. Relpose: Predicting probabilistic relative rotation for single objects in the wild. In *Proceedings of European Conference on Computer Vision (ECCV)*, page 592–611, 2022. [1](#)
- [44] Jason Y Zhang, Amy Lin, Moneish Kumar, Tzu-Hsuan Yang, Deva Ramanan, and Shubham Tulsiani. Cameras as rays: Pose estimation via ray diffusion. In *Proceedings of International Conference on Learning Representations (ICLR)*, 2024. [1](#), [5](#), [8](#)